Blueprint Academic Publishers

Journal of Aquatic and Terrestrial Ecosystems
Journal ISSN: 2960-1118
4(3)
Received: September 14, 2026
Accepted: October 19, 2026
Published: October 29, 2026

Valorization of Sugarcane Bagasse into Amorphous Graphenic Nanocomposites for Sustainable Aqueous Hexavalent Chromium Remediation

Makokha Grace*, Wambu W. Enos and Kituyi Lusweti John

Department of Chemistry and Biochemistry, School of Science, University of Eldoret, P.O Box 1125 -30100, Eldoret, Kenya

Abstract

Global industrialization has severely contaminated aquatic ecosystems with highly toxic, carcinogenic hexavalent chromium Cr(VI), creating critical public health and ecological crises. Yet, current wastewater treatment methods are plagued by significant operational limitations such as high treatment costs, high energy consumption, and the creation of toxic secondary sludge. This study aims to synthesize a functional, amorphous graphenic nanocomposite (AGN) from sugarcane bagasse via an energy-efficient, low-temperature (300°C), single-stage catalytic pyrolysis method to achieve sustainable and cost-effective aqueous Cr(VI) remediation. An AGN was synthesized by blending sugarcane bagasse with a ferrocene catalyst (5:1 w/w), pyrolyzing at a low temperature of 300 °C for 20 minutes, and washing with 5% HCl. The resulting material was characterized using X-ray diffraction (XRD), scanning electron microscopy (SEM), and Fourier-transform infrared spectroscopy (FTIR). Finally, the Cr(VI) removal performance of the AGN was evaluated through batch adsorption tests across varying adsorbent dosages, pH levels, contact times, agitation speeds, and initial Cr(VI) concentrations, with residual Cr(VI) concentrations measured via atomic absorption spectrophotometer (AAS). Hexavalent Cr removal was highly pH-dependent, achieving maximum efficiency at pH 1.0 below the material's pH point of zero charge (pH_{pzc} = 4.5), but dropping to near 0% above pH 7.0. Increasing the adsorbent dosage to 1.6 g yielded a modest maximum efficiency of 24%. The equilibrium data fitted the Langmuir isotherm (R^2 = 0.9248), demonstrating monolayer chemisorption with a low maximum adsorption capacity of 0.2921 mg/g. The pseudo-first-order model was used to fit the adsorption kinetics and yielded R^2 = 0.9373, and k_1 = 0.0548 min^{-1}, indicating rapid initial transport. Mechanistically, removal is facilitated by electrostatic interactions between $HCrO_4^-$ and protonated –OH and C–O networks, complex intercalation into the graphitic galleries and localized surface coordination. Ultimately, this one-step catalytic pyrolysis is an energy-efficient route for valorizing sugarcane bagasse into

a low-cost nanomaterial, and it provides a fundamentally sustainable, circular-economy process framework for agricultural waste recycling and wastewater remediation.

Keywords: Adsorption isotherms, chromium, environmental remediation, environmental water pollution, graphene oxide synthesis, kinetics, sugarcane bagasse

Corresponding Author: **Makokha** *gracamak@gmail.com

Wambu: ewambu@uoeld.ac.ke

Kituyi: joluki@yahoo.com

Copyright © 2026 Makokha et al. This is an open-access article distributed under the terms of the Creative Commons Attribution License (CC BY).

Funding: The author received no financial support for the research, authorship and/or publication of this article.

Data Availability: The author confirm that the supporting findings of this study are available within the article and/ or its supplementary material or upon request.

Conflict of interest: The authors declare that there is no potential conflict of interest with respect to the research authorship and /or publication of this article.

Competing interests: The author declares no potential conflicts of interest with respect to the research, authorship and/or publication of this article.

1. Introduction

The recent surge in global industrialization rate has greatly accelerated the release of toxic heavy metals into aquatic environments, and the contamination of water with Cr(VI) is now a major concern for human health and environmental safety. Large quantities of chromium-containing wastewater are regularly discharged from industrial processes, including leather tanning, chrome plating, textile dyeing, wood preservation, chromate production and metallurgical alloy manufacturing (Islam et al., 2023; Khatua & Kumar Dey, 2023; Xie, 2024). In the environment, chromium primarily exists as trivalent chromium [Cr(III)] and Cr(VI). Cr(III) is comparatively less toxic and is known to be an essential trace micronutrient for basic cellular metabolism, but it has low water solubility and bioavailability (Acharyya et al., 2023; Islam et al., 2023; Khatua & Kumar Dey, 2023). Its long-term risk, however, is its potential to change into the more stable chemically or biologically highly toxic Cr(VI) form under certain environmental conditions (Islam et al., 2023; Khatua & Kumar Dey, 2023; Rasool et al., 2026; Zulfiqar et al., 2023). In contrast, Cr(VI) is a highly corrosive, mobile and mutagenic carcinogen that can cause severe damage to the kidneys and liver due to its high water solubility, fluidity, permeability, and high oxidation potential, which is known to produce strong oxidative stress and severe genotoxicity within biological cells, leading to histone degradation, disruption

of base pairing in DNA, and the alteration of entire chromosomal assemblies (Islam et al., 2023; Khatua & Kumar Dey, 2023; Xie, 2024).

In view of these potential risks, the World Health Organization has set a strict limit of 0.05 mg/L for Cr in drinking water (World Health Organization, 2008). Nonetheless, anthropogenic point sources of Cr pollution continue to cause significant pollution of fresh water, with documented ecological crises occurring all over East Africa, mostly due to pollution from the production of industrial wooden posts (Acharyya et al., 2023; Khatua & Kumar Dey, 2023). Specifically, these include, among others, the violation of critical statutory limits in the Ethiopian River Koche (Temesgen et al., 2024) and high concentrations of heavy metals in industrial and urban areas in Kenya (Munene et al., 2023; Murphy et al., 2025; Musungu et al., 2025). In recent monitoring, for example, substantial levels of Cr contamination in tannery effluents and surrounding soils, as well as hotspots of Cr(VI) in urban boreholes and industrial belts, such as Nairobi and Kwale, have been detected, which exceed regulatory safety limits (Musungu et al., 2025; Oruko et al., 2021).

There are major operational limitations associated with scaling up traditional physical, chemical, and membrane separation methods for aqueous Cr cleanup (Islam et al., 2023; Konradt et al., 2023; Xie, 2024). Specifically, chemical precipitation requires significant amounts of chemicals and results in large quantities of toxic metal sludge that must be disposed of as hazardous waste (Singhal et al., 2026; Xie, 2024) . Ion exchange resins, although highly efficient kinetically, suffer from high operating costs, complicated regeneration, and fast fouling waste (Singhal et al., 2026; Xie, 2024). In addition, these high-efficiency membrane filtration processes are highly energy-consuming, easily get clogged, and produce toxic, highly concentrated retentate streams (Khatua & Kumar Dey, 2023; Konradt et al., 2023; Xie, 2024). At the same time, conventional activated carbon filtration quickly loses retention capacity after repeated cycles because mineral precipitates block and deactivate the crucial surface sites (Konradt et al., 2023).

To address this environmental challenge, a novel sustainable and cost-effective remediation solution using stable carbonaceous nanostructures derived from abundant and cheap agricultural biomass such as sugarcane bagasse is emerging, which not only addresses the problems of agro-waste disposal but, it also promotes the circular economy (Akhtar et al., 2024; Dermawan et al., 2025; Hiranobe et al., 2024; Mahawong et al., 2025; Thangaraj et al., 2023). However, the conventional methods of synthesizing graphitic or activated carbon generally involve high temperatures, high energy consumption, or corrosive chemical activation agents, which come with a heavy economic and environmental cost. This makes it imperative to develop scientific routes to restructure raw biomass into tailored nanocomposites with minimal alteration to the natural surface functionality, using green and low-temperature processes.

In this regard, the present work proposes the synthesis of an AGN obtained by the single-stage catalytic pyrolysis of sugarcane bagasse, offering exceptional technical and energetic novelty. Unlike energy-intensive conventional biochar or synthetic graphene production that requires temperatures between 600 °C and 900 °C for hours, performing the pyrolysis at 300 °C for just 20 minutes drastically lowers the thermal energy footprint (da Silva et al., 2023; Hiranobe et al., 2024;

Prasannamedha & Kumar, 2022). This one-step reaction can directly incorporate Fe species into the carbon matrix, avoiding the use of complicated multi-step carbon activation reactions and thereby promoting low-temperature carbon aromatization and template graphitization (Dermawan et al., 2025; Mahawong et al., 2025). Importantly, the preservation of a dense array of oxygen-containing functional groups (–COOH, –OH, C–O) in the disordered graphenic nanosheets was achieved without the extreme deoxygenation and thermal degradation associated with higher temperatures (Akhtar et al., 2024; Prasannamedha & Kumar, 2022).

2. Materials and Methods

2.1 Materials and Equipment

Sugarcane bagasse was collected from the Nzoia Sugar Factory (Bungoma County, Kenya). The raw biomass was washed repeatedly with doubly deionized water (DDW) to remove surface impurities, dried in an electric oven at 70 °C for three hours, and subsequently pulverized using a mechanical grinder. All chemical reagents utilized in this study were of analytical grade and procured from Sigma-Aldrich (St. Louis, USA).

Phase separation during the adsorption runs was achieved using a Centurion 6000 series centrifuge (Centurion Scientific Ltd, West Sussex, UK), while sample agitation was maintained using a Cole-Parmer™ Stuart™ orbital shaker (Illinois, USA). The residual concentrations of Cr(VI) ions were quantified via an AAS (AAS, Model AA-60, China). To characterize the structural, morphological, and surface properties of the synthesized material, XRD patterns were recorded on a Bruker D8 Advance diffractometer (Bruker AXS, Karlsruhe, Germany), surface morphologies were examined using a TESCAN VEGA S5123 SEM (SEM, Brno, Czech Republic), and FTIR spectral profiles were acquired using a WQF-520 FTIR spectrophotometer (Beijing, China).

2.2 Procedure

2.2.1 Synthesis of Amorphous Graphenic Nanocomposite

The synthesis of the AGN was based on a modified catalytic pyrolysis process (Somanathan et al., 2015). A 2.5 g sample of preheated bagasse was mechanically blended with 0.5 g of a ferrocene organometallic catalyst (5:1 w/w ratio) in a ceramic crucible. The mixture was placed in a muffle furnace, heated to a low-temperature regime of 300 °C, and isothermally held for 20 min. After the synthesized material had cooled to room temperature, the dark carbonaceous matrix was dispersed in 100 mL of 5% (v/v) HCl and stirred vigorously for 12 h. This acid washing was conducted to remove active iron species and to facilitate the formation of surface functionalities containing oxygen. The suspension was filtered, and the resulting residue was washed repeatedly with DDW until a neutral pH was attained. The final product was dried at 100 °C for 12 h and stored in a sealed container. The procedure was repeated in batches to accumulate a sufficient yield for subsequent testing.

2.2.2 Adsorbent Characterization

XRD profiling was carried out with an X-ray diffractometer operated with a Cu Kα source (λ = 1.5406 Å) at 40 kV and 30 mA. Diffraction spectra were measured within the 2θ scanning range of 5-80° at a scan rate of 2° min^{-1}. Microstructural and morphological analyses were conducted by mounting the finely ground AGN on conductive carbon tape, sputter-coating it with a thin layer of gold, and then imaging through SEM at 5-20 kV accelerating

voltage across various magnifications. The surface functional groups were tracked using FTIR spectroscopy within a wavenumber range of 400 to 4000 cm^{-1} at a spectral resolution of 4 cm^{-1} over an accumulation of 20 scans.

2.2.3 Batch Adsorption Tests

The synthesized AGN was tested for the removal of Cr(VI) using batch adsorption runs to investigate the effect of operational parameters such as adsorbent dosage (0.05–3.2 g/50 mL), agitation speed (70–190 rpm), contact time (1.0–320 min), initial solution pH (2.0–12.0), and initial Cr(VI) ion concentration (1.0–200 mg/L). Typically, a 50 mL aliquot of the specified aqueous Cr(VI) solution was brought into contact with a predetermined mass of AGN inside Erlenmeyer flasks under preset experimental conditions. The batches were then agitated and centrifuged; the clear supernatant was subsequently analyzed by AAS to determine the remaining equilibrium concentration of Cr. The equilibrium adsorption capacity (q_e, mg/g) and the percentage removal efficiency (% Removal) were computed using Equations (1) and (2), respectively

$$q_e = \frac{C_i - \mathrm{C_f}}{m} \times v \qquad (1)$$

$$\%\ Removal = \frac{C_f - \mathrm{C_i}}{\mathrm{C_f}} \times 100 \qquad (2)$$

where, the variables are defined as follows: q_e is the equilibrium adsorption capacity (mg/g), C_i and C_f are the initial and final metal ion concentrations (mg/L), respectively, v is the batch volume (L), and m is the adsorbent mass (g).

Furthermore, pHpzc for the AGN was determined using pH Drift Method. A 0.1 M sodium chloride (NaCl) solution was utilized as the background inert electrolyte to maintain a constant ionic strength (Gutierrez et al., 2023).

2.2.4 Data Analysis and Presentation

The data were subjected to analysis by computing the mean and the standard deviation of replicate measurements. Graphical regression analysis was used to explore possible casual relationships and determine correlation coefficients.

3. Results

3.1 Characterization of Pristine and Metal-Ion-Loaded AGN

3.1.1 XRD Analysis

The XRD pattern of AGN is shown in Fig. 1, a broad peak is observed at 26.24° (2θ), corresponding to the (002) crystallographic plane of graphitic carbon, which is characteristic of highly disordered, amorphous graphenic material (Zerin et al., 2025). Conversely, a minor diffraction peak is observed at ~12.36° (2θ), yielding an interlayer d-spacing of 0.7064 nm that matches the layered domains typical of this adsorbent material. Following Cr(VI) sorption, a clear downward shift in these peaks was noted.

3.1.2 SEM Analysis

The morphological characteristics of the pristine and Cr-loaded AGN are not clearly distinguishable via scanning electron microscopy (SEM) analysis (Fig. 2). The pristine AGN presents a characteristic partially exfoliated, layered nanosheet architecture with wrinkled surfaces, irregular edges, and intersheet voids (Idris et al., 2022; Kumar et al., 2022) as shown in Fig. 2a–b. The high-magnification imaging (Fig. 2b) reveals that these nanosheets exhibit significant folds and deformations, resulting from the disruption of the graphitic lattice during the preceding oxidation process (Akhtar et al., 2024; Emon et al., 2025). After Cr loading, the morphology of the AGN is not significantly altered, exhibiting only limited Cr binding to the AGN matrix (Fig. 2c–d).

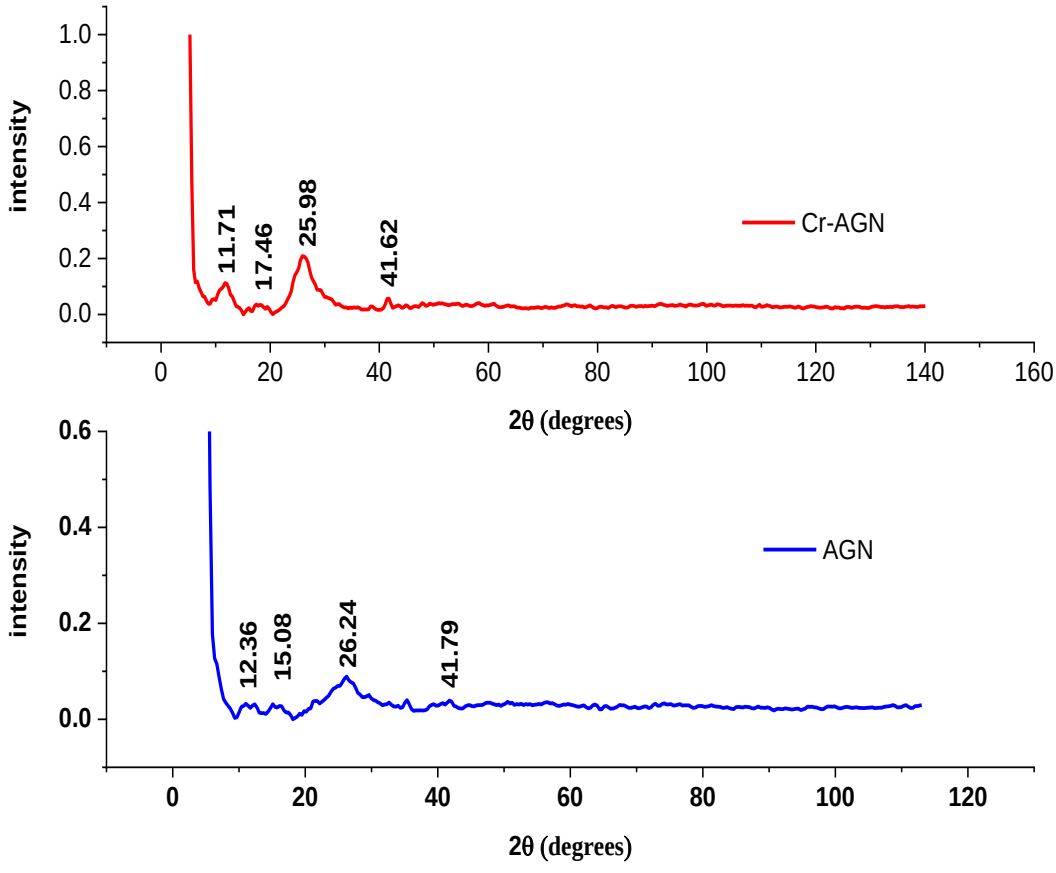
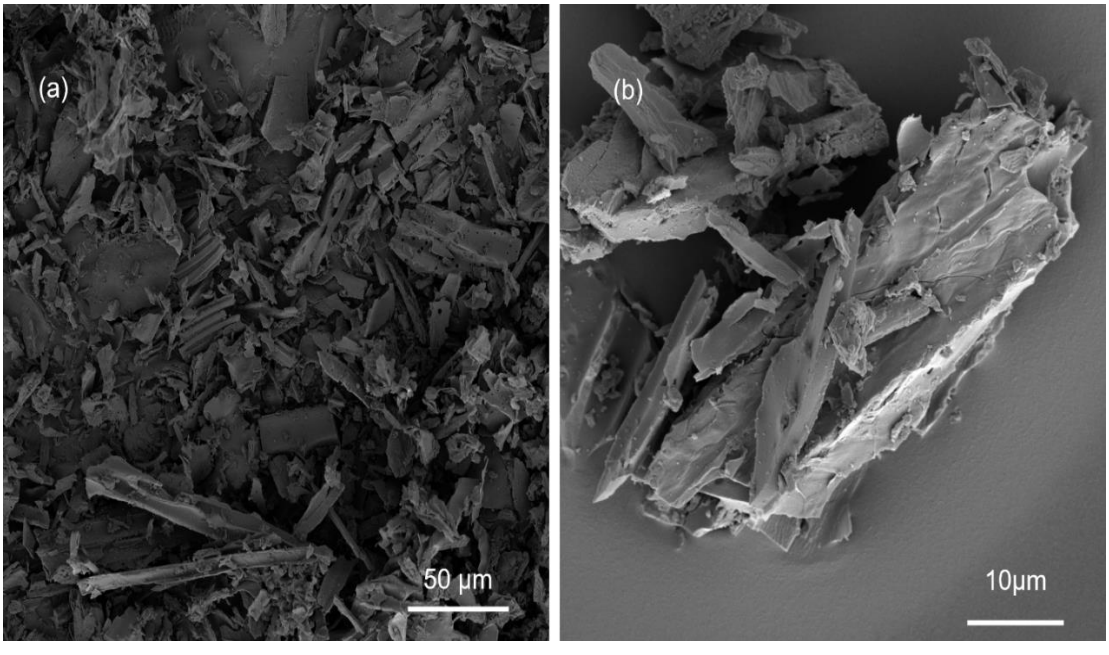


Figure 1. X-ray diffraction pattern of AGN, and Cr-loaded AGN



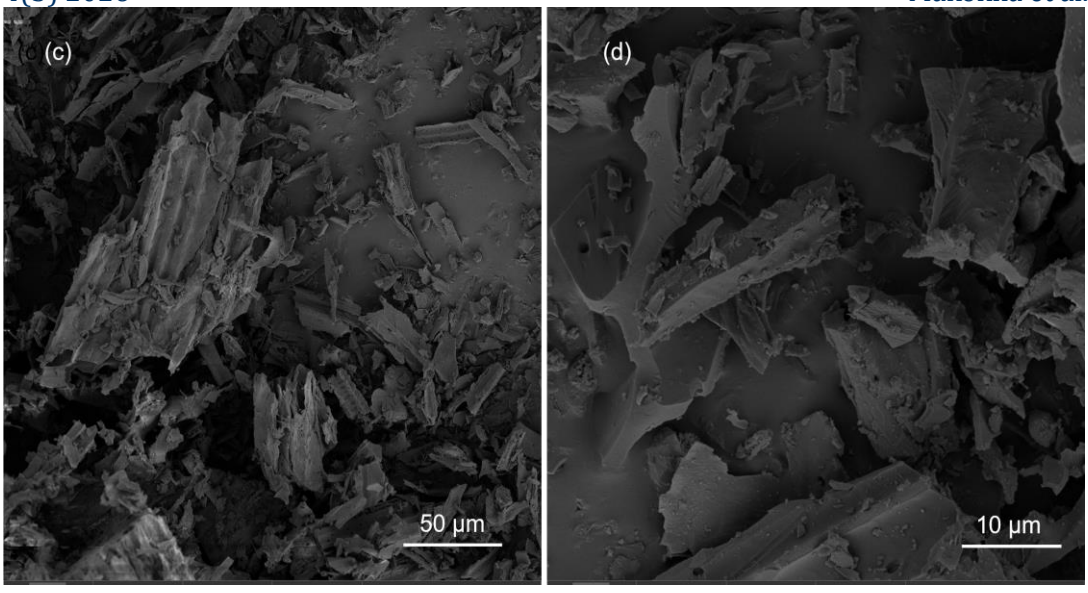


Figure 2. SEM micrographs of pristine and Cr-loaded AGN at different magnifications: (a–b) pristine AGN; (c–d) Cr-loaded AGN.

3.1.3 FTIR Analysis

The FTIR spectra of pristine, and Cr-loaded AGN are displayed in Fig. 3

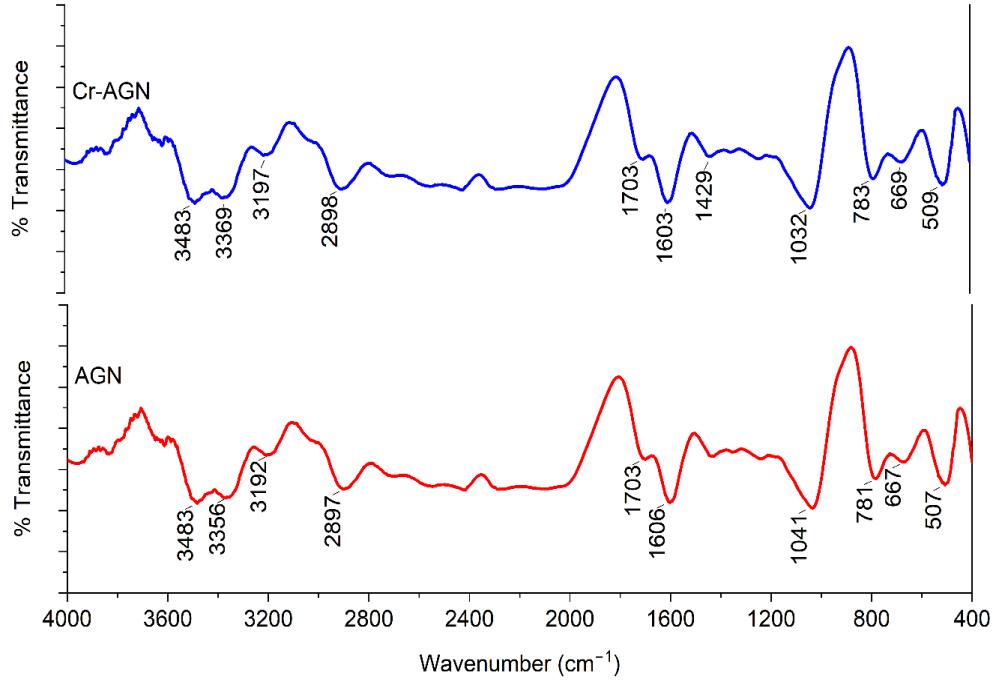


Figure 3. The FTIR spectra of AGN, and Cr-loaded AGN

Spectral profiles confirm the successful conversion of sugarcane bagasse to GO-based nanocomposites, indicating the presence of various functional groups, such as hydroxyl (–OH), carboxyl (C=O), aromatic ring (C=C), and

alkoxy (C–O), with characteristic peaks at 3483–3356, 1703, 1606, and 1041 cm^{-1}, respectively. Additionally, peaks at 2897 and 781 cm^{-1} represent C–H stretching (Ali, 2018; Biswas et al., 2025; de Barros et al., 2023; Kumar et al., 2025).

Shifts in key functional groups were observed following Cr sorption on the AGN matrix. The broad –OH stretching band shifted from 3483–3356 cm^{-1} to 3483–3369 cm^{-1}, while the C=C network vibrations moved from 1606 cm^{-1} to 1603 cm^{-1}. Concurrently, the C–O stretching bands shifted from 1041 cm^{-1} to 1032 cm^{-1}, and the out-of-plane aromatic C–H bending vibrations shifted from 781 cm^{-1} to 783 cm^{-1}.

In contrast, other structural markers remained stationary; for instance, the aliphatic C–H stretching bands showed negligible variation, moving only from 2897 cm^{-1} to 2898 cm^{-1}. Furthermore, the C=O stretching peaks associated with carboxylic acid or ketone functionalities remained completely unchanged at 1703 cm^{-1}.

3.2 Effect of pH on Cr Adsorption

As illustrated in Fig. 4, Cr(VI) removal by the AGN matrix was highly pH-dependent, reaching its maximum at pH 1.0 and dropping to near 0% at pH > 7. The pH_{pzc} for the adsorbent was found to be 4.5, explaining the suppressed adsorption in alkaline conditions.

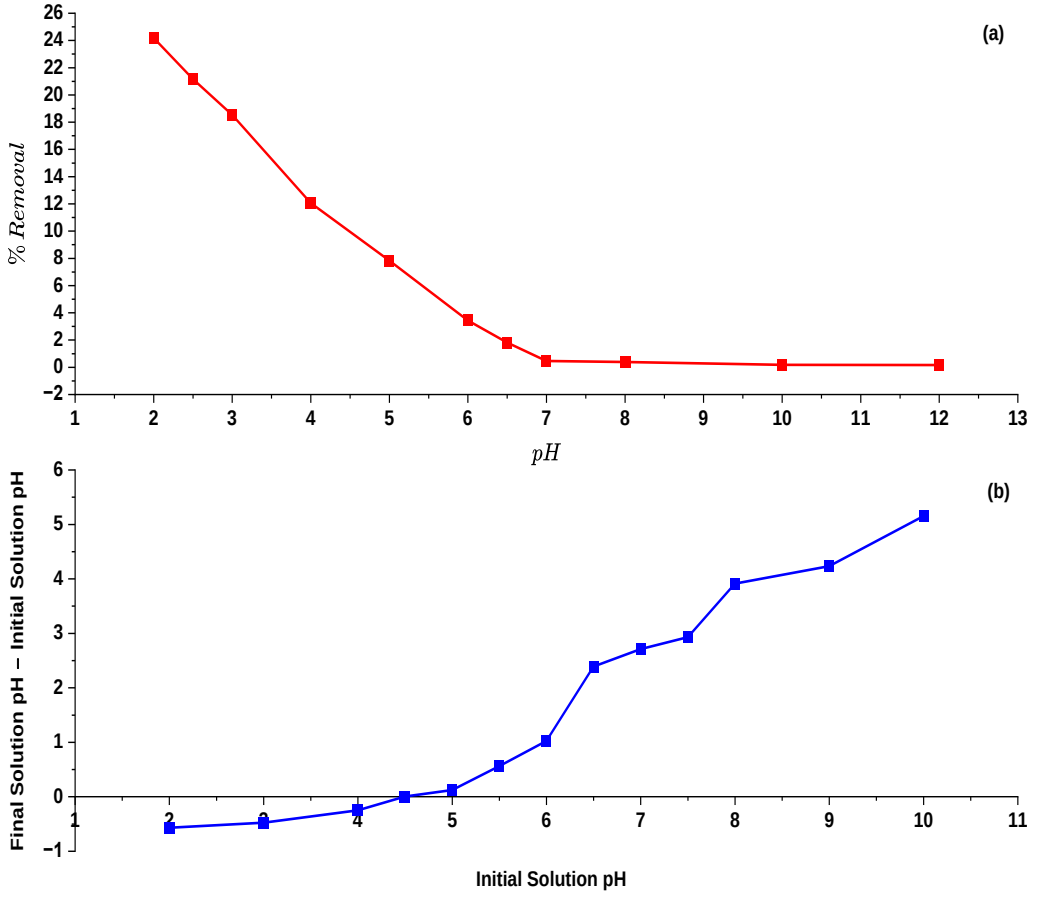


Figure 4. Results of pH effect and pH_{pzc} of AGN using the pH drift method (Conditions: adsorbent dosage = 1.6 g/50 mL; agitation speed = 100 rpm; initial adsorbate concentration =10 mg/L; temperature = 298K; background electrolyte = 0.1 M NaCl equilibration time = 24 h)

3.3 Effect of Changes in Mass of Adsorbent

The influence of AGN adsorbent dosage (0.05–3.2 g) on Cr(VI) uptake is depicted in Fig. 5.

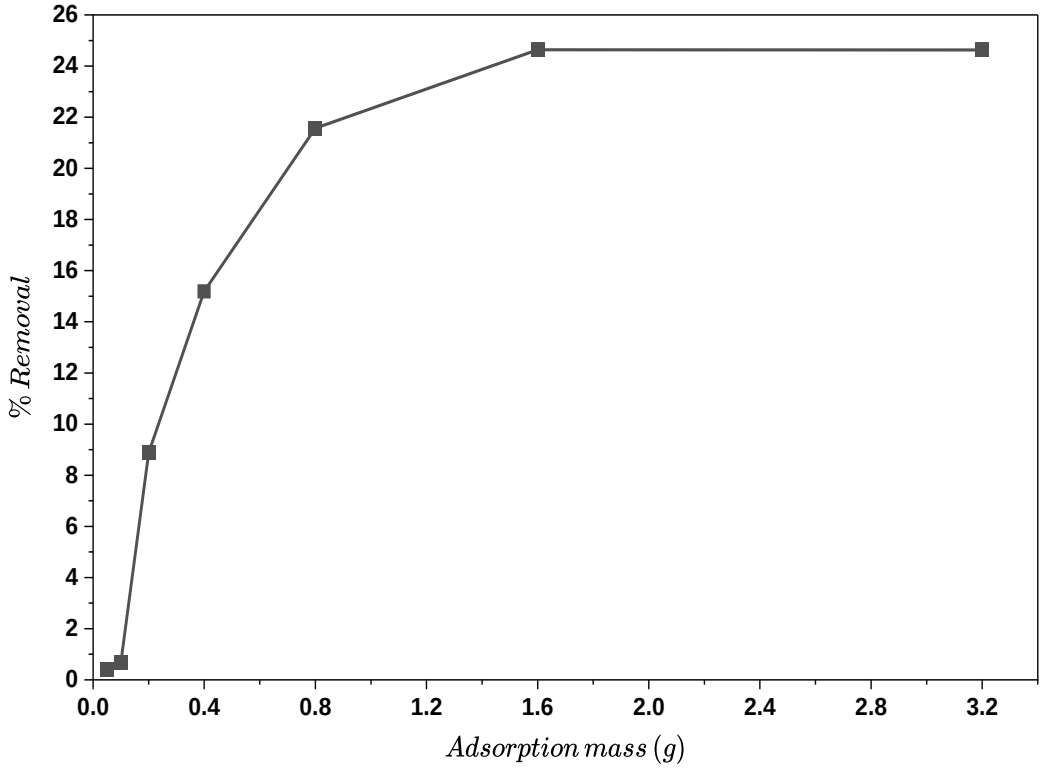


Figure 5. Result of varying adsorbent mass (0.05–3.2 g): batch volume 50 mL, adsorbate concentration 10 mg/L, agitation rate 100 rpm, contact time 4 h, temperature 298 K, pH 1.0

Chromium removal efficiencies were remarkably low, yielding less than 1% adsorption at the lowest adsorbent dose of 0.05 g. Even with an increased AGN dosage, the Cr(VI) removal efficiency remained highly limited, peaking at only 24% when the dosage was raised to 1.6 g.

3.4 Effect of Agitation Rate

The effect of agitation speed (70–190 rpm) on Cr(VI) removal from aqueous media is illustrated in Fig. 6. The removal of Cr(VI) by AGN was highly dependent on the agitation speed, although the overall adsorption efficiency remained low. At the lowest agitation speed of 70 rpm, AGN achieved a 12% Cr(VI) removal efficiency. Raising the agitation speed from 70 to 100 rpm improved removal, reaching approximately 23%. Increasing the agitation speed beyond 100 rpm, however, yielded no further improvement in Cr(VI) removal, suggesting that the system had reached equilibrium or a transport-limited stage.

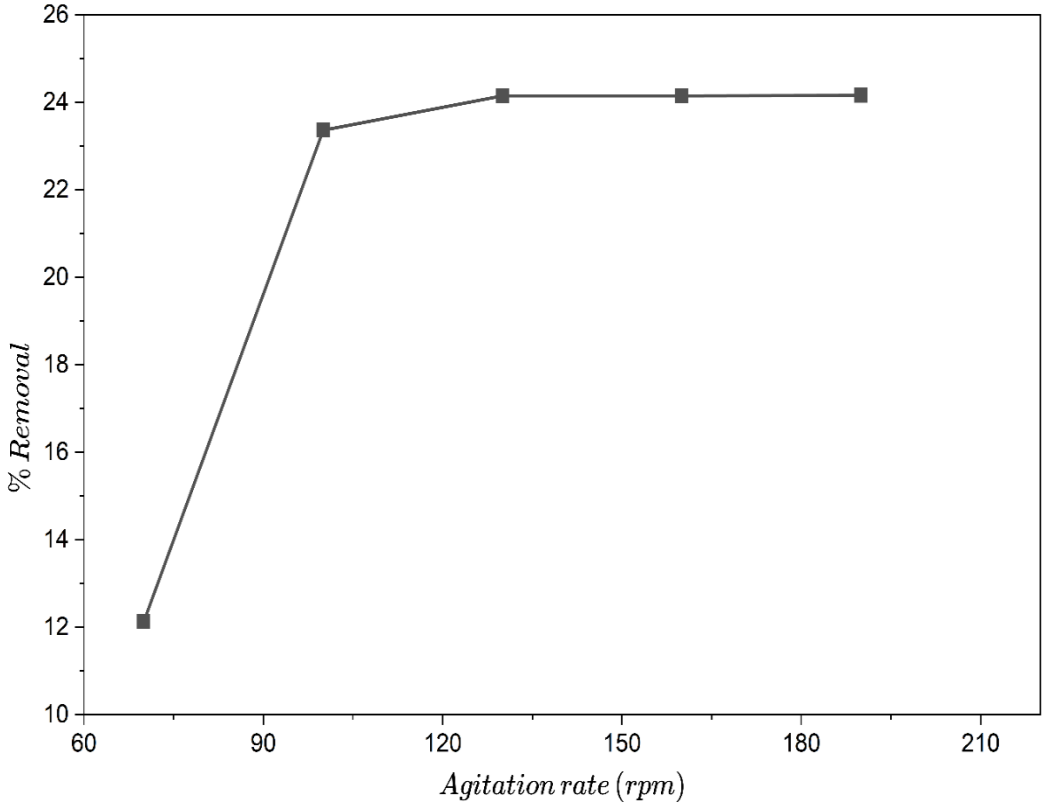


Figure 6. Effect of varying agitation rate (70–190 rpm). 50 mL batch volume, 10 mg/L initial adsorbate concentrations, 4 h contact time, 298 K temperature, 1.6 g adsorbent dosage, pH 1.0

3.5 Contact Time and Adsorption Kinetics

Chromium(VI) uptake by AGN was observed as a function of contact time (1–160 min) and was modeled using standard kinetic equations. Lagergren pseudo-first-order (Eq. 3), Ho's pseudo-second-order (Eq. 4), and Weber-Morris intra-particle diffusion (Eq. 5) models (Ho & McKay, 1999; Lagergren, 1898; Weber & Morris, 1963) were used in the following forms:

$$\log (q_e - q_t) = \log q_e - \left(\frac{k_1}{2.303}\right) t \quad (3)$$

$$\frac{t}{q_t} = \frac{1}{k_2\, q_e^2} + \frac{t}{q_e} \quad (4)$$

$$q_t = \frac{k_w}{m}\, t^{0.5} + C \quad (5)$$

where, q_e (mg/g) and q_t (mg/g) refer to the adsorption capacities at equilibrium and at time t (min), respectively. The variables k_1 (min^{-1}), k_2 (g. mg^{-1}. min^{-1}), and k_w (mg/g. min$^{0.5}$) are the rate constants of the pseudo-first-order, pseudo-second-order, and intra-particle diffusion models, respectively; the intercept (C, mg/g) represents boundary layer effects, and m (g) is the mass of the adsorbent.

The effect of contact time and the corresponding linear regression fits are summarized in figure 7, and all derived kinetic constants are presented in Table 1.

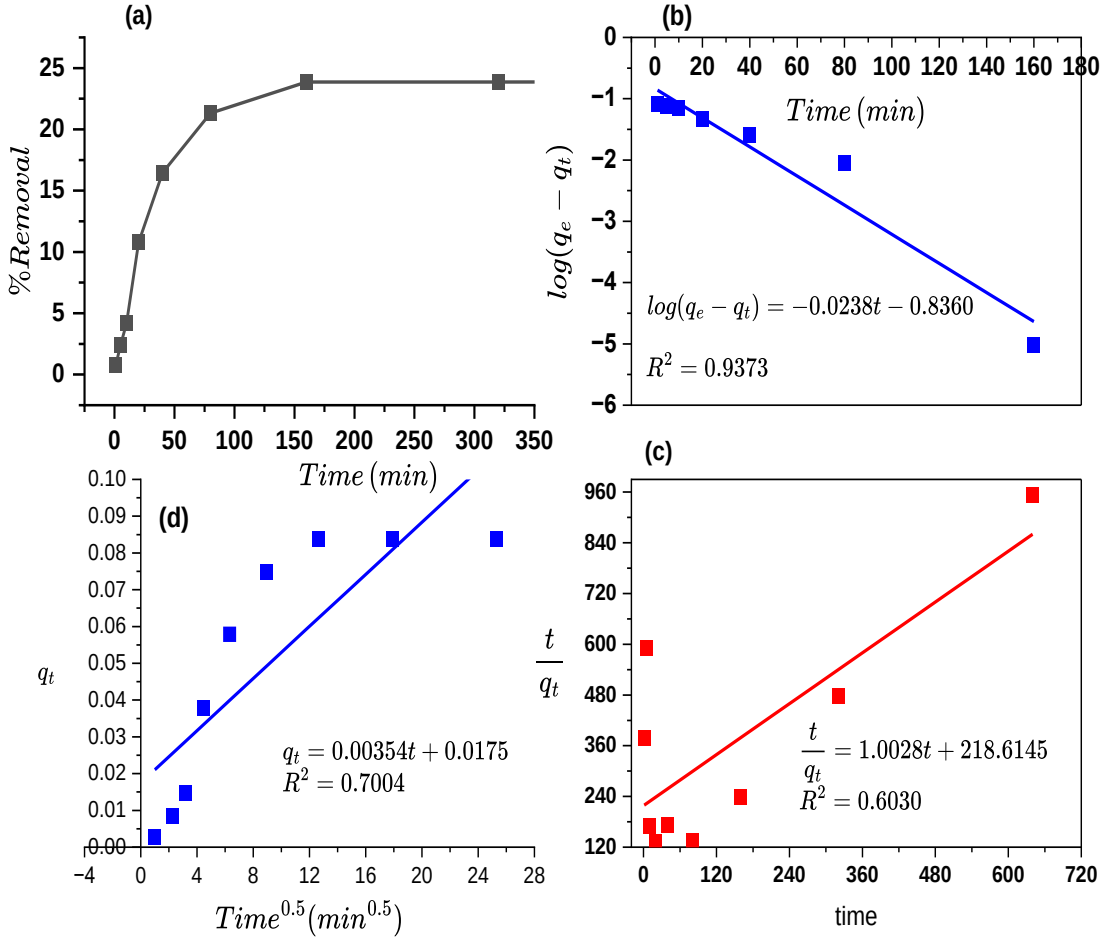


Figure 7. Adsorption time profile for Cr(VI) on AGN showing (a) the effect of adsorption contact time, (b) the Lagergren pseudo-first-order, (c) Ho's pseudo-second-order, and (d) Intra-particle diffusion kinetics plots

Table 1. Kinetic model parameters and coefficients of determination for Cr(VI) adsorption onto AGN

Lagergren's pseudo-first order			**Ho's pseudo-second order**			**Weber-Morris intra-particle diffusion**		
k_1	(Min^{-1})	0.0548	k_2	(g/mg/min)	0.0046	K_w	(mg/g. $min^{0.5}$)	0.00354
q_e	(mg/g)	0.1459	q_e	(mg/g)	0.9972	C	(mg/g)	0.0175
R^2		0.9373	R^2		0.6030	R^2		0.7004

3.6 Initial Concentration and Adsorption Isotherm Analysis

To investigate the effect of initial Cr(VI) concentration on its adsorption onto AGN, a concentration range of 1 to 200 mg/L was utilized, as shown in Figure 8. At the lowest evaluated initial Cr(VI) concentration of 1.6075 mg/L, the removal efficiency was remarkably low, with only 26% of the Cr(VI) removed from the aqueous solution. As the initial adsorbate concentration increased beyond this point, a sharp significant decline in the Cr(VI) adsorption was observed.

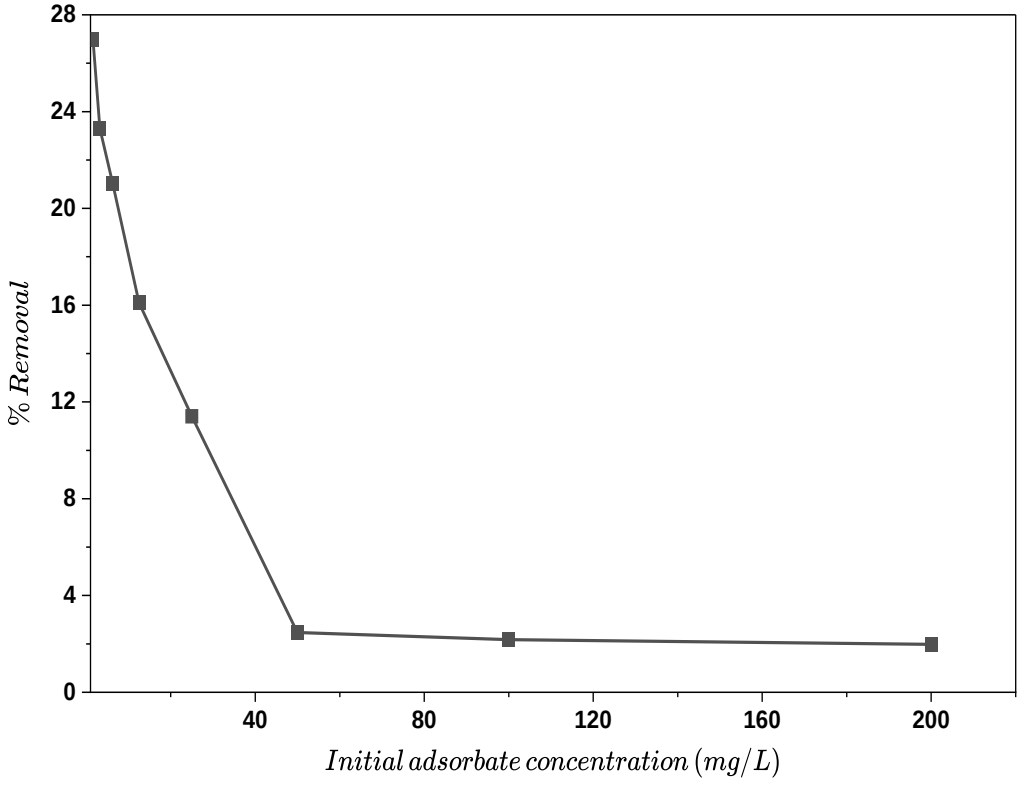


Figure 8. Effect of initial Cr(VI) concentration (1.6–200 mg/L) on adsorption onto AGN. Experimental conditions: batch volume = 50 mL, adsorbent dosage = 1.6 g, agitation rate = 100 rpm, contact time = 160 min, pH = 1.0, temperature = 298 K

The Cr(VI) uptake by AGN was modeled using the linearized Langmuir (Eq. 6) and Freundlich (Eq. 7) isotherms (Freundlich, 1907; Langmuir, 1918)

$$\frac{1}{q_e} = \frac{1}{bq_m C_e} + \frac{1}{q_m} \quad (6)$$

$$\log q_e = \log K_f + \frac{1}{n}\log C_e \quad (7)$$

where, C_e (mg/L) is the equilibrium concentration of Cr(VI), q_e (*mg/g*) is the amount adsorbed at equilibrium, then q_m (mg/g) is the Langmuir adsorption capacity, whereas, K_f (mg/g.(L/mg)$^{1/n}$ and n are the Freundlich constants. The isotherm plots and derived parameters are presented in Figure 9 and Table 2.

Based on the Langmuir plot, the calculated maximum monolayer adsorption capacity (q_m) was found to be 0.2921 mg/g, and the Langmuir adsorption affinity constant (b) was 0.0721 L/mg. Concurrently, the Freundlich linear regression yielded an adsorption intensity parameter (n) of 2.2904 and a Freundlich adsorption capacity constant (K_f) of 0.0391 mg/g.(L/mg)$^{1/n}$ (Table 2).

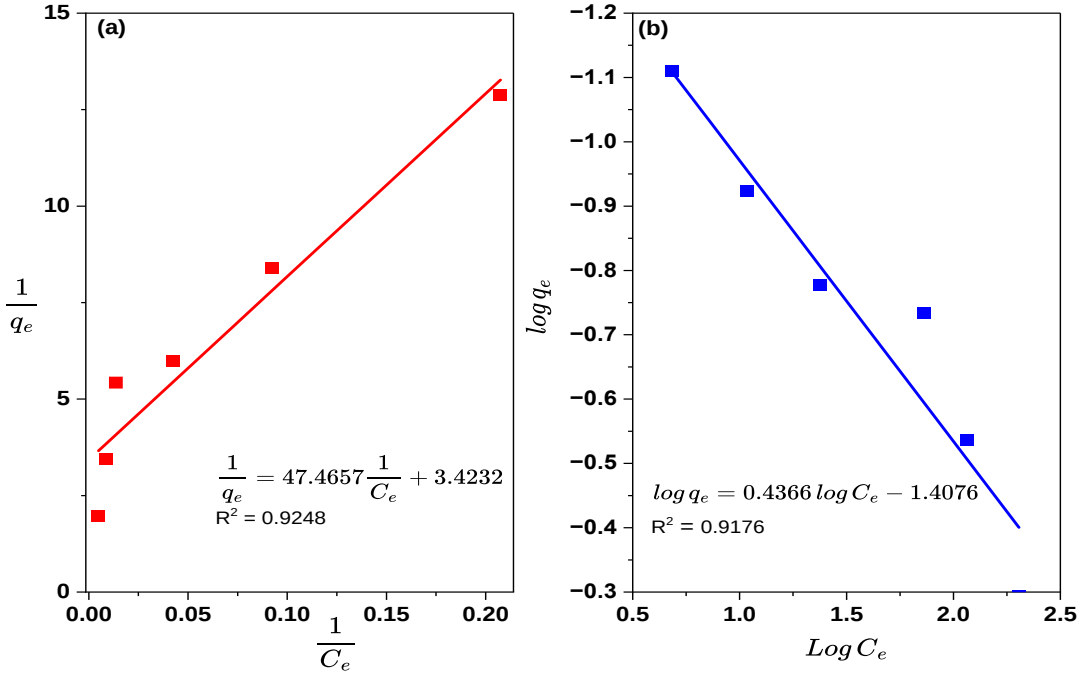


Figure 9. Linearized Langmuir (a) and Freundlich (b) isotherm plots for Cr(VI) adsorption onto AGN

Table 2. Langmuir and Freundlich isotherm parameters for the sorption of Cr(VI) onto AGN

Langmuir Parameters			**Freundlich Parameters**	
q_m	(mg/g)	0.2921	K_f(mg/g.(L/mg)$^{1/n}$	0.0391
b	(L/mg)	0.0721	n	2.2904
R^2		0.9248	R^2	0.9176

4. Discussion

4.1 Characterization of AGN and AGN-loaded Cr(VI)

The evidence obtained via X-ray diffraction analysis of the material after Cr(VI) uptake was crucial for understanding structural changes and spatial intercalation. The downward shifts in the XRD peaks after Cr uptake–specifically moving from 12.36° to 11.71°, 26.24° to 25.98°, and 41.79° to 41.62°–are consistent with an increase in d-spacing. This dilation is caused by interfacial coordination and partial intercalation into oxygen-rich nanospaces, rather than simple surface coating alone (Li et al., 2021; Ren et al., 2025; Rouzière et al., 2018). This lattice dilation provides clear, direct evidence of the intercalation of Cr complexes into the inner galleries of the graphitic nanosheets (Acharya et al., 2021; Islam et al., 2019; Tadjenant et al., 2020).

The preservation of the partially exfoliated nanosheet morphology after adsorption shows that Cr(VI) capture is a phenomenon restricted to the surface, which agrees with the low q_m of 0.2921 mg/g. No visible changes could be detected via SEM, but molecular-level interactions were confirmed by the FTIR vibrational changes.

The modification of the broad –OH bands (3483–3356 to 3483–3369 cm^{-1}), the shifts in the C–O (1041 to 1032 cm^{-1}), and the changes in the C=C (1606 to

1603 cm^{-1}) demonstrate that Cr coordination is strictly restricted to these specific oxygen-containing and graphenic domains (Abenojar et al., 2024; Khdoor et al., 2024; Naseem et al., 2022). Importantly, the C=O peak in the carbonyl region is completely unaffected, indicating that the carboxylic acid/ketone functional groups are not involved in the coordination chemistry. Moreover, the low-frequency shift between 781 and 783 cm^{-1} corresponds to out-of-plane aromatic C–H bending deformations, suggesting that the overall structure of the graphenic backbone remains intact during the sorption process. This highly localized, non-participatory interaction of important functional groups—specifically the carbonyls—offers a clear molecular explanation for the low adsorption capacity.

4.2 Effect of Solution pH Cr(VI) sorption on AGN

The solution pH exerts profound control over the surface charge of the AGN matrix and the chemical speciation of Cr in an aqueous environment. Maximum adsorption occurred at pH 1.0, with near 0% removal at pH > 7. At an extremely acidic level like pH 1.0, Cr(VI) predominantly exists as the highly stable, mobile anionic hydrogen chromate ($HCrO_4^-$) or neutral chromic acid (H_2CrO_4) (El-Nemr et al., 2025; Yuan et al., 2023), while the abundance of H^+ ions intensively protonates the adsorbent surface groups (Abewaa et al., 2024). The pH_{pzc} of the AGN matrix was determined to be 4.5, providing a clear thermodynamic rationale for this behavior. When the solution pH is maintained well below this point (pH < 4.5), the adsorbent surface gains a net positive charge due to the protonation of the –OH networks and C–O centers (Abewaa et al., 2024). This positive surface potential exerts a strong electrostatic attraction toward anionic chromate complexes. Conversely, as the solution pH moves beyond 4.5 (pH > pH_{pzc}), these surface protons are systematically removed, creating a negative charge on the deprotonated layered domains. This leads to a very strong electrostatic repulsion of anionic Cr species, such as the chromate ion (CrO_4^{2-}), which causes the dramatic drop in performance (El-Nemr et al., 2025; Tattibayeva et al., 2022).

4.3 Effect of Adsorbent Dosage

Evaluating the effect of mass variations showed that the percentage removal increased with an increasing adsorbent mass, reaching a maximum efficiency of 24% at about 1.6 g dosage. This positive correlation between mass and removal percentage is mathematically tied to the absolute number of binding sites. Introducing more adsorbent into the system increases the total surface area and multiplies the active functional groups available for coordination (Ali et al., 2023; Din et al., 2026). However, the modest maximum efficiency of 24% at 1.6 g confirms that a substantial portion of these newly added domains remains unutilized or geometrically blocked (Tan et al., 2024). This closely aligns with the SEM data showing tight structural folding and nanosheet deformation, which likely induced active site overlapping and particle aggregation at higher solid-to-liquid ratios (Din et al., 2026; El-Nemr et al., 2025; Rahdar et al., 2026), thereby hindering further extraction.

4.4 Effect of Agitation Rate

The external mass transfer was largely controlled by hydrodynamic conditions; for example, when the agitation speed was increased from 70 to 100 rpm, the percentage removal rose, though no further uptake was observed

with increased agitation beyond 100 rpm. This reduction in boundary layer film resistance around the partially exfoliated nanosheets improved the transport of Cr(VI) ions from the bulk solution to the wrinkled surfaces and irregular edges of the sheets (Bin Bandar & Aljlil, 2023; Elgarahy et al., 2023). Once the system reached the critical threshold of 100 rpm, external film diffusion resistance was completely overcome (Elgarahy et al., 2023; García-Hernández et al., 2022). At velocities higher than this, the entire process was dominated by intraparticle pore diffusion and surface chemisorption at –OH and C–O coordination sites, causing the adsorption to plateau (Wu et al., 2026) . This performance plateau was driven not only by internal coordination kinetics (Abdel Hameed et al., 2026; Ibrahim et al., 2026; Parimelazhagan et al., 2022) but also by the depletion of available functional binding sites and the disappearance of boundary layer concentration gradients (Ibrahim et al., 2026; Parimelazhagan et al., 2022).

4.5 Effect of Initial Adsorbate Concentration and adsorption Isotherms

The baseline system achieved only 26% Cr removal at the lowest initial concentration of 1.6075 mg/L, and increasing the initial adsorbate concentration caused a decrease in the percentage uptake. The low uptake at this initial concentration (~1.6mg/L) is due to a low driving force from the minimal concentration gradient for mass transfer from the solution toward the graphitic functional groups, which balances boundary layer diffusion (Singh et al., 2024; Yuan et al., 2023). The absolute capacity (q_e) is usually enhanced as the initial concentration is raised, due to the resulting steeper concentration gradient. The percentage removal, however, decreased because the exfoliated but distorted graphitic structure readily fills the available binding sites, resulting in saturation. Additionally, structural defects or sub-optimal surface protonation may limit baseline binding (Gao et al., 2023; Kang et al., 2022; Umejuru et al., 2023).

Equilibrium modeling provides key information about the surface configuration and surface interactions of the AGN matrix. The Langmuir isotherm provided a better fit for the experimental data (R^2 = 0.9248; q_m = 0.2921 mg/g, and b = 0.0721 L/mg) than the Freundlich model (R^2 = 0.9176; K_f = 0.0391, and n = 2.2904). This statistical preference proves that Cr uptake proceeds via uniform chemisorption on a limited number of identical functional groups (Billah et al., 2026; He et al., 2026; Meretoudi et al., 2025). This aligns with FTIR data showing that interactions are focused on specific active binding centres (–OH, C–O, and C=C domains) rather than random multilayer adsorption or void entrapment (Gürsoy et al., 2025; Manzoor et al., 2024; Rahdar et al., 2026). Concurrently, intact skeletal C–H vibrations confirm the structural integrity (He et al., 2026; Laranja et al., 2022) of the graphenic framework (Manzoor et al., 2024; Rahdar et al., 2026). The low adsorption capacity is caused by: incomplete carbonization and low porosity from pyrolysis at 300 °C (He et al., 2026; Laranja et al., 2022) ; HCl leaching which removes catalytic iron reduction sites (Dermawan et al., 2025); and insufficient basic heteroatoms that limit the quantity of protonated adsorption sites (Laranja et al., 2022; Manzoor et al., 2024).

4.6 Adsorption Kinetics

The experimental kinetic data conformed satisfactorily to the pseudo-first-order (PFO) model, yielding a rate constant of k_1 = 0.0548 min^{-1} and a correlation coefficient of (R^2 = 0.9373). This relatively high k_1 value signifies a rapid initial migration rate, which is

significantly accelerated by the strong coulombic attraction between the highly protonated graphitic active groups (at pH 1.0 < pH_{pzc} of 4.5) and the anionic Cr species. Conversely, the pseudo-second-order (PSO) model provided an inferior fit (k_2 = 0.0046 g/ mg. min, and R^2 = 0.6030), confirming that the overall rate-limiting step is not governed by progressive, bimolecular electron-sharing chemisorption. While PSO models traditionally dominate chemically functionalized systems, PFO pathways frequently prevail in carbonaceous nanocomposites when the kinetics are mediated by rapid electrostatic physisorption and physical surface transport boundaries (Liu et al., 2022; Naseem et al., 2022). This initial electrostatic trapping rapidly occupies a finite, uniform set of exposed binding sites on the carbon framework, leading to spatial site saturation as validated by the Langmuir isotherm fit (Gonfa et al., 2025; Pazoki & Anbia, 2025; Singh et al., 2024). Furthermore, the intraparticle diffusion model displayed a moderate correlation (k_w = 0.00354 mg/ (g. $min^{0.5}$, R^2 = 0.7004). The notable non-zero intercept (C) quantifies a substantial boundary layer film resistance operating at the external solid–liquid interfaces (Liu et al., 2022; Tibebu et al., 2024; Umejuru et al., 2023). This external interface limitation structurally correlates with the slight structural contractions observed in the matrix lattice, as evidenced by the downward shifting of XRD peaks.

4.7 Adsorption Mechanism

The kinetic, structural, equilibrium, and surface chemical data were combined to propose a comprehensive adsorption mechanism. High agitation speeds (Bin Bandar & Aljlil, 2023; Elgarahy et al., 2023) control the hydrodynamic film transport at the beginning of the process, followed by fast, pseudo-first order surface transport into the matrix. Extensive protonation of surface –OH (3483–3356 cm^{-1}), and C–O networks (1041 cm^{-1}) exerts a strong electrostatic attraction toward anionic $HCrO_4^-$ under highly acidic conditions (pH 1.0 < pH_{pzc}) (Abewaa et al., 2024). These complexes are not merely deposited as external crusts, as demonstrated by the unaltered SEM matrix topology, but instead actively penetrate the internal galleries (Abdel Hameed et al., 2026; Wu et al., 2026). The characteristic downward shift of the XRD peaks is attributed to this structural entry, which leads to an increase in the interlayer d-spacing.

Finally, the Cr ions are immobilized through localized complexation/coordination, hydrogen bonding, and cation–π interactions with the electron-rich graphitic framework (Acharya et al., 2021; Islam et al., 2019; Tadjenant et al., 2020). The sorption of Cr typically occurs through a combination of electrostatic attraction of the hydrated $HCrO_4^-$ anion, followed by reduction to CrO_4^{2-} and coordination to the functional groups, and any dilation can be attributed to either of the two processes (Acharya et al., 2021; Islam et al., 2019; Tadjenant et al., 2020). The most robust mechanistic restriction is the low probability of a fully hydrated Cr(VI) sorbed ion persisting; many Cr(VI) systems are reduced to Cr(III) on the surface, with the generated Cr(III) being present as coordinated Cr–O species, amorphous $Cr(OH)_3$-like domains or inner-sphere complexes (He et al., 2026; Jiang et al., 2014; Rajapaksha et al., 2018).

5. Conclusions

An AGN was successfully synthesized from sugarcane bagasse using a green synthetic method. This approach provides a sustainable and cost-effective strategy for agricultural waste recycling

and circular-economy resource valorization.

Batch adsorption tests indicated that the removal of Cr(VI is significantly pH-dependent, with the maximum efficiency achieved at a pH of 1.0 and decreasing to near 0% when the pH is above 7.0.

The Langmuir isotherm model yielded the better fit for the equilibrium data (R^2 = 0.9248), which indicates that a monolayer chemisorption mechanism occurred. The material, however, exhibited a low maximum adsorption capacity of 0.2921 mg/g.

The adsorption kinetics were found to adhere to pseudo-first-order adsorption model with R^2 = 0.9373 and k_1 = 0.0548 min^{-1}, which indicates rapid initial transport of Cr(VI) ions.

From a mechanistic point of view, Cr(VI) removal is driven by electrostatic interactions between $HCrO_4^-$ anions and protonated –OH and C–O surface networks, supported by complex intercalation into the graphitic galleries and localized surface coordination.

Overall, while the low-temperature pyrolysis route is energy-efficient, optimization is required to increase its practical remediation capacity.

6. Future Recommendations

Investigate chemical activation or surface functionalization to create more active binding sites and improve the low adsorption capacity.

Optimize low-temperature pyrolysis parameters, such as variations in temperature (350°C–400°C) and biomass-to-catalyst ratios, to increase the specific surface area and improve the graphitic pore network.

Conduct adsorption-desorption cycles to assess the reusability, long-term stability, and economic viability of the AGN adsorbent for industrial use.

Evaluate the adsorbent's performance using real industrial wastewater to determine its selectivity and effectiveness toward Cr(VI) when competing, co-existing ions are present.

References

Abdel Hameed, S. E., Abou El-Maaty, W. M., Gomaa, E. A., & Awad, F. S. (2026). PAR-intercalated Mg/Al layered double hydroxide for efficient adsorption of acid fuchsin: experimental study and molecular docking insights. *RSC Advances*, *16*(7), 6408–6420. https://doi.org/10.1039/D5RA08890A

Abenojar, J., López de Armentia, S., del Real, J. Carlos., & Martinez, M. A. (2024). Magnetic cork as adsorbent to remove hexavalent chromium from aqueous solution. *Applied Water Science*, *14*(12), 267. https://doi.org/10.1007/s13201-024-02322-z

Abewaa, M., Arka, A., Haddis, T., Mengistu, A., Takele, T., Adino, E., Abay, Y., Bekele, N., Andualem, G., & Girmay, H. (2024). Hexavalent chromium adsorption from aqueous solution utilizing activated carbon developed from Rumex abyssinicus. *Results in Engineering*, *22*, 102274. https://doi.org/10.1016/j.rineng.2024.102274

Acharya, R., Lenka, A., & Parida, K. (2021). Magnetite modified amino group-based polymer nanocomposites towards efficient adsorptive detoxification of aqueous Cr(VI): A review. *Journal of Molecular Liquids*, *337*, 116487. https://doi.org/10.1016/j.molliq.2021.116487

Acharyya, S., Das, A., & Thaker, T. P. (2023). Remediation processes of hexavalent chromium from groundwater: a short review. *AQUA — Water Infrastructure, Ecosystems and Society*, *72*(5), 648–662. https://doi.org/10.2166/aqua.2023.123

Akhtar, M. S., Jutt, D. S. R., Aslam, S., Nawaz, R., Irshad, M. A., Khan, M., Khairy, M., Irfan, A., Al-Hussain, S. A., & Zaki, M. E. A. (2024). Green synthesis of graphene oxide and magnetite nanoparticles and their arsenic removal efficiency from arsenic contaminated soil. *Scientific Reports*, *14*(1), 23094. https://doi.org/10.1038/s41598-024-73734-9

Ali, A. H., Kareem, A. B., Al-Rawi, U. A., Khalid, U., Zhang, S., Zafar, F., Papraćanin, E., Hatshan, M. R., & Sher, F. (2023). Kinetic and equilibrium study of graphene and copper oxides modified nanocomposites for metal ions adsorption from binary metal aqueous solution. *Frontiers in Chemistry*, *11*. https://doi.org/10.3389/fchem.2023.1279948

Ali, M. E. A. (2018). Synthesis and adsorption properties of chitosan-CDTA-GO nanocomposite for removal of hexavalent chromium from aqueous solutions. *Arabian Journal of Chemistry*, *11*(7), 1107–1116. https://doi.org/10.1016/j.arabjc.2016.09.010

Billah, Md. M., Rabbi, S. M. F., Kamruzzaman, Md., Hoque, M. A., Bhuiyan, R. H., & Nisa, I. J. (2026). Sustainable Congo red (CR) and hexavalent chromium Cr(VI) removal using graphene functionalized aminated lignin composite: mechanistic and reusability insights. *RSC Advances*, *16*(16), 14378–14394. https://doi.org/10.1039/D5RA08641H

Bin Bandar, K., & Aljlil, S. (2023). Utilization of prepared nanocellulose as a biopolymer for adsorption kinetics of cobalt ions from wastewater. *Polymers*, *15*(9), 2143. https://doi.org/10.3390/polym15092143

Biswas, S. S., Kundu, A. K., Biswas, H. S., & Maiti, D. K. (2025). Solvothermal synthesis and comprehensive characterization of high-quality graphene oxide. *Journal of Nano- and Electronic Physics*, *17*(4), 04017-1-04017–5. https://doi.org/10.21272/jnep.17(4).04017

da Silva, C. M. S., Oliveira, M. L. S., Manera, C., Godinho, M., Perondi, D., Ahmad, N., Nawaz, A., Silva, L. F. O., & Dotto, G. L. (2023). From grape bagasse to graphene-like porous carbon nanosheets for CO^2 capture. *Environmental Science and Pollution Research*, *30*(53), 113481–113493. https://doi.org/10.1007/s11356-023-30427-6

de Barros, N. G., Gonzaga Neto, A. C., Vaccioli, K. B., Angulo, H. R. V., de Andrade e Silva, L. G., Toffoli, S. M., & Valera, T. S. (2023). Graphene Oxide: A Comparison of Reduction Methods. *C-Journal of Carbon Research*, *9*(3). https://doi.org/10.3390/c9030073

Dermawan, D., Satriavi, A. D., Nurhidayati, D. I., Firnandi, R., Mayangsari, N. E., Ramadani, T. A., Widiana, D. R., Juniani, A. I., Mujiyanti, D. R., & Wang, Y.-F. (2025). Composite adsorbent from sugarcane (Saccharum officinarum) bagasse biochar generated from atmospheric pressure microwave plasma pyrolysis process and nano zero valent iron (nZVI) for rapid and highly efficient Cr(VI) adsorption. *Case Studies in Chemical and Environmental Engineering*, *11*, 101123. https://doi.org/10.1016/j.cscee.2025.101123

Din, S. U., Al-Ahmary, K. M., Al-Mhyawi, S. R., AlMohamadi, H., Elamin, N. Y., Alshdoukhi, I. F., Imohiosen, F. A., Ofudje, E. A., & Al-Otaibi, J. S. (2026). Sustainable removal of Cd(II) and Cr(VI) from aqueous solution via agro-waste derived biochar. *Scientific Reports*, *16*(1), 9792. https://doi.org/10.1038/s41598-026-40608-1

Elgarahy, A. M., Mostafa, H. Y., Zaki, E. G., ElSaeed, S. M., Elwakeel, K. Z., Akhdhar, A., & Guibal, E. (2023). Methylene blue removal from aqueous solutions using a biochar/gellan gum hydrogel

composite: Effect of agitation mode on sorption kinetics. *International Journal of Biological Macromolecules*, *232*, 123355. https://doi.org/10.1016/j.ijbiomac.2023.123355

El-Nemr, M. A., Aigbe, U. O., Ukhurebor, K. E., Obodo, K., Awe, A. A., Hassaan, M. A., Ragab, S., & El Nemr, A. (2025). Modelling of a new form of nitrogen doped activated carbon for adsorption of various dyes and hexavalent chromium ions. *Scientific Reports*, *15*(1), 3896. https://doi.org/10.1038/s41598-025-87398-6

Emon, S. H., Hossain, M. I., Khanam, M., & Yi, D. K. (2025). Expanding horizons: Taking advantage of graphene's surface area for advanced applications. *Applied Sciences*, *15*(8), 4145. https://doi.org/10.3390/app15084145

Freundlich, H. (1907). Über die Adsorption in Lösungen. *Zeitschrift Für Physikalische Chemie*, *57U*(1), 385–470. https://doi.org/10.1515/zpch-1907-5723

Gao, F., Zhang, L., Yang, L., Zhou, X., & Zhang, Y. (2023). Structural properties of graphene oxide prepared from graphite by three different methods and the effect on removal of Cr(VI) from Aqueous Solution. *Nanomaterials*, *13*(2), 279. https://doi.org/10.3390/nano13020279

García-Hernández, E., Aguilar-Madera, C. G., Herrera-Hernández, E. C., Flores-Cano, J. V., Bailón-García, E., González, A. T. F., Aguilar-Aguilar, A., & Ocampo-Pérez, R. (2022). 3D modeling of the adsorption rate of pyridine on activated carbon cloth in a stirred tank under turbulent conditions. *Processes*, *10*(4), 735. https://doi.org/10.3390/pr10040735

Gonfa, G., Kidanu, A., Akram, S., Lal, B., Kezembayeva, G., Bokov, D. O., Asghari, A., Yadav, K. K., Saravanan, A., & Hosseini-Bandegharaei, A. (2025). Adsorptive removal of Cr(VI) from water using silver nanoparticle modified-diatomite nanocomposite. *Scientific Reports*, *15*(1), 41993. https://doi.org/10.1038/s41598-025-25998-y

Gürsoy, S., Zeytinci, N. K., Zaman, B. T., Bakırdere, S., & Öztürk Er, E. (2025). Study of linear and nonlinear isotherm and kinetic parameters of hexavalent chromium adsorption onto reduced graphene oxide coated iron oxide. *Scientific Reports*, *15*(1), 25206. https://doi.org/10.1038/s41598-025-97588-x

Gutierrez, A. M., Dziubla, T. D., & Hilt, J. Z. (2023). The impact of solution ionic strength, hardness, and pH on the sorption efficiency of polychlorinated biphenyls in Magnetic Nanocomposite Microparticle (MNM) Gels. *Gels*, *9*(4), 344. https://doi.org/10.3390/gels9040344

He, J., Meng, B., Qi, H., Fan, H., Long, M., Yu, M., Bao, X., & Zhang, L. (2026). Pyrolysis temperature-driven structural evolution of wheat straw biochar and enhanced adsorption mechanisms for Cr(VI). *RSC Advances*, *16*(22), 20103–20116. https://doi.org/10.1039/D6RA00077K

Hiranobe, C. T., Gomes, A. S., Paiva, F. F. G., Tolosa, G. R., Paim, L. L., Dognani, G., Cardim, G. P., Cardim, H. P., dos Santos, R. J., & Cabrera, F. C. (2024). Sugarcane bagasse: Challenges and opportunities for waste recycling. *Clean Technologies*, *6*(2), 662–699. https://doi.org/10.3390/cleantechnol6020035

Ho, Y. S., & McKay, G. (1999). Pseudo-second order model for sorption processes. *Process Biochemistry*, *34*(5), 451–465. https://doi.org/10.1016/S0032-9592(98)00112-5

Ibrahim, I. M., Turky, A. M., Mostafa, N. Y., & Roushdy, M. H. (2026). Valorization of ductile cast iron solid waste as a high-performance adsorbent for crystal violet removal:

characterization, optimization, and mechanistic insights. *RSC Advances*, *16*(27), 24427–24453. https://doi.org/10.1039/D6RA02129H

Idris, A. O., Orimolade, B. O., Potlako, M., Feleni, U., Nkambule, T. T. I., & Mamba, B. B. (2022). Exfoliated graphite: A surface renewed electrode for environmental applications. *Frontiers in Sensors*, *3*. https://doi.org/10.3389/fsens.2022.861965

Islam, M. M., Mohana, A., Rahman, Md. A., Rahman, M., Naidu, R., & Rahman, M. M. (2023). A comprehensive review of the current progress of chromium removal methods from aqueous solution. *Toxics*, *11*. https://doi.org/10.3390/toxics11030252

Islam, Md. A., Angove, M. J., & Morton, D. W. (2019). Recent innovative research on chromium(VI) adsorption mechanism. *Environmental Nanotechnology, Monitoring & Management*, *12*, 100267. https://doi.org/10.1016/j.enmm.2019.100267

Jiang, W., Cai, Q., Xu, W., Yang, M., Cai, Y., Dionysiou, D. D., & O'Shea, K. E. (2014). Cr(VI) adsorption and reduction by humic acid coated on magnetite. *Environmental Science & Technology*, *48*(14), 8078–8085. https://doi.org/10.1021/es405804m

Kang, Z., Gao, H., Hu, Z., Jia, X., & Wen, D. (2022). Ni–Fe/reduced graphene oxide nanocomposites for hexavalent chromium reduction in an aqueous environment. *ACS Omega*, *7*(5), 4041–4051. https://doi.org/10.1021/acsomega.1c05273

Khatua, S., & Kumar Dey, S. (2023). The chemistry and toxicity of chromium pollution: An overview. *Asian Journal of Agricultural and Horticultural Research*, *10*(2), 1–14. https://doi.org/10.9734/ajahr/2023/v10i2221

Khdoor, Z., Makharza, S., Qurie, M., Fohely, F., Abu Taha, A., & Hampel, S. (2024). Removal of toxic hexavalent chromium via graphene oxide nanoparticles: study of kinetics, isotherms, and thermodynamics. *RSC Advances*, *14*(34), 24345–24351. https://doi.org/10.1039/D4RA03697B

Konradt, N., Dillmann, S., Becker, J., Schroden, D., Rohns, H.-P., Wagner, C., Müller, U., Konradt, D., Janknecht, P., Hobby, R., ElSherbiny, I. M. A., & Panglisch, S. (2023). Removal of chromium species from low-contaminated raw water by different drinking water treatment processes. *Water*, *15*(3), 516. https://doi.org/10.3390/w15030516

Kumar, P., Gupta, M., Hawari, H. F., Kumar, V., & Mishra, Y. K. (2025). Chemical and surface modification in graphene oxide for optimum CO^2 gas sensing performance. *Nano Express*, *6*(2), 25004. https://doi.org/10.1088/2632-959X/adc758

Kumar, H. V, Oyer, A. J., Huang, K. Y.-S., & Adamson, D. H. (2022). Evolution of heterogeneity and chemical functionality during the oxidation of graphite. *Colloids and Interfaces*, *6*(3), 44. https://doi.org/10.3390/colloids6030044

Lagergren, S. (1898). Zur Theorie der sogenannten adsorption gelöster stoffe. *Kungliga Svenska Vetenskapsakademiens Handlingar*, *24*(4), 1–39

Langmuir, I. (1918). The adsorption of gases on plane surfaces of glass, mica and platinum. *Journal of the American Chemical Society*, *40*(9), 1361–1403. https://doi.org/10.1021/ja02242a004

Laranja, M. J., Júnior, F. H., Nogueira, G. A., Vieira, L. H., Oliveira, N. C., Soares, J. M., Cordeiro, C. H., Otubo, L., Moreira, A. B., Ferreira, O. P., & Bisinoti, M. C. (2022). Valorisation of sugar cane bagasse using hydrothermal carbonisation in the preparation of magnetic carbon nanocomposite in a single-step

synthesis applied to chromium adsorption. *Journal of Chemical Technology & Biotechnology*, *97*(8), 2032–2046. https://doi.org/10.1002/jctb.7074

Li, Z., Wang, R., Wu, S., Xue, Z., Zhu, D., Zou, J., & Li, X. (2021). In situ observation of metal ion interactions with graphene oxide layers: From the growth of metal hydroxide to metal oxide formation. *Carbon*, *184*, 721–727. https://doi.org/10.1016/j.carbon.2021.08.073

Liu, Y., Shan, H., Zeng, C., Zhan, H., & Pang, Y. (2022). Removal of Cr(VI) from wastewater using graphene oxide chitosan microspheres modified with α–FeO(OH). *Materials*, *15*(14), 4909. https://doi.org/10.3390/ma15144909

Mahawong, S., Onsri, P., Thaveemas, P., Kaowphong, S., Nijpanich, S., Rattanachueskul, N., Techasakul, S., Chuenchom, L., & Dechtrirat, D. (2025). Transforming waste into value: Single-step in situ synthesis of magnetic porous carbon composite adsorbents from sugarcane bagasse and iron scrap. *Scientific Reports*, *15*(1), 16098. https://doi.org/10.1038/s41598-025-00610-5

Manzoor, Q., Farrukh, M. A., Qamar, M. T., Sajid, A., Aldossari, S. A., Manikandan, A., & Iqbal, M. (2024). Polymer-assisted synthesis of ternary magnetic graphene oxide nanocomposite for the adsorptive removal of Cr(VI) and Pb(II) ions. *Heliyon*, *10*(15), e35204. https://doi.org/10.1016/j.heliyon.2024.e35204

Meretoudi, A. D., Tolkou, A. K., Kosheleva, R. I., Xanthopoulou, M., Tzollas, N. M., Kostoglou, M., Katsoyiannis, I. A., & Kyzas, G. Z. (2025). Carrageenan@Graphene Oxide nanocomposites for the adsorption of trivalent arsenic, hexavalent chromium, and fluoride ions from aqueous solutions: Conceptualization modeling of adsorptive interfacial interactions, kinetics, and swelling. *Langmuir*, *41*(25), 16529–16547. https://doi.org/10.1021/acs.langmuir.5c01927

Munene, E. N., Hashim, N. O., & Ambusso, W. N. (2023). Human health risk assessment of heavy metal concentration in surface water of Sosian river, Eldoret town, Uasin-Gishu County Kenya. *MethodsX*, *11*, 102298. https://doi.org/10.1016/j.mex.2023.102298

Murphy, M., Wachira, G., Onyango, C., & Hoffmann, V. (2025). Heavy metal contamination in urban agriculture: evidence from Nairobi. *Environmental Science and Pollution Research*, *32*(44), 25231–25245. https://doi.org/10.1007/s11356-025-37030-x

Musungu, H., Mosonik, B. C., & Kibet, J. K. (2025). A comprehensive review of heavy metal contamination in selected boreholes and their impact on water quality management in Kenya. *Discover Water*, *5*(1), 121. https://doi.org/10.1007/s43832-025-00320-z

Naseem, T., Bibi, F., Arif, S., Waseem, M., Haq, S., Azra, M. N., Liblik, T., & Zekker, I. (2022). Adsorption and kinetics studies of Cr(VI) by graphene oxide and reduced graphene oxide-zinc oxide nanocomposite. *Molecules*, *27*(21), 7152. https://doi.org/10.3390/molecules27217152

Oruko, R. O., Edokpayi, J. N., Msagati, T. A. M., Tavengwa, N. T., Ogola, H. J. O., Ijoma, G., & Odiyo, J. O. (2021). Investigating the chromium status, heavy metal contamination, and ecological risk assessment via tannery waste disposal in sub-Saharan Africa (Kenya and South Africa). *Environmental Science and Pollution Research*, *28*(31), 42135–42149. https://doi.org/10.1007/s11356-021-13703-1

Parimelazhagan, V., Yashwath, P., Arukkani Pushparajan, D., & Carpenter, J.

(2022). Rapid removal of toxic remazol brilliant blue-r dye from aqueous solutions using Juglans nigra shell biomass activated carbon as potential adsorbent: Optimization, isotherm, kinetic, and thermodynamic investigation. *International Journal of Molecular Sciences*, *23*(20), 12484. https://doi.org/10.3390/ijms232012484

Pazoki, H., & Anbia, M. (2025). Kinetic and isotherm studies of Cr(VI) adsorption from aqueous media by using a synthetic chitosan-allophane nanocomposite. *Scientific Reports*, *15*(1), 11088. https://doi.org/10.1038/s41598-024-72839-5

Prasannamedha, G., & Kumar, P. S. (2022). Hydrothermal carbonization of waste sugarcane bagasse for the effective removal of emerging contaminants from aqueous solution. *Adsorption Science & Technology*, *2022*. https://doi.org/10.1155/2022/8684737

Rahdar, S., Davoudi, M., Shams, M., & Dehghan, A. A. (2026). Environmentally sustainable renewable luffa-derived biomass graphene nanosheets for efficient Cr(VI) removal: Fabrication, characterization, and adsorption analysis. *Scientific Reports*, *16*(1), 21039. https://doi.org/10.1038/s41598-026-51369-2

Rajapaksha, A. U., Alam, Md. S., Chen, N., Alessi, D. S., Igalavithana, A. D., Tsang, D. C. W., & Ok, Y. S. (2018). Removal of hexavalent chromium in aqueous solutions using biochar: Chemical and spectroscopic investigations. *Science of The Total Environment*, *625*, 1567–1573. https://doi.org/10.1016/j.scitotenv.2017.12.195

Rasool, A., Pertile, E., Brožová, K., Halfar, J., Čabanová, K., Malíková, P., Chromíková, J., Motyka, O., Drabinová, S., & Heviánková, S. (2026). Mechanistic insights and environmental ramifications of Cr(III) oxidation to Cr(VI) in soil and groundwater systems: bridging geochemical mechanisms and emerging remediation strategies. *Environmental Geochemistry and Health*, *48*(1), 12. https://doi.org/10.1007/s10653-025-02901-2

Ren, X., Lin, T., Sun, B., Ramadhan, Z. R., Yin, H., Hussain, F., Dai, Q., Tilley, R., Dai, L., Gu, Z., & Joshi, R. (2025). Electrostatically induced intercalation of layered double hydroxide in graphene oxide for enhanced electrochemical energy storage. *Advanced Science*, *12*(48). https://doi.org/10.1002/advs.202515923

Rouzière, S., Launois, P., Benito, A. M., Maser, W. K., & Paineau, E. (2018). Unravelling the hydration mechanism in a multi-layered graphene oxide paper by in-situ X-ray scattering. *Carbon*, *137*, 379–383. https://doi.org/10.1016/j.carbon.2018.05.043

Singh, S., Anil, A. G., Uppara, B., Behera, S. K., Nath, B., N, P., Bhati, S., Singh, J., Khan, N. A., & Ramamurthy, P. C. (2024). Adsorption and DFT investigations of Cr(VI) removal using nanocrystals decorated with graphene oxide. *Npj Clean Water*, *7*(1), 17. https://doi.org/10.1038/s41545-024-00306-9

Singhal, P., Sharma, V., Kumar, R., Alkhanjaf, A. A. M., Umar, A., & Baskoutas, S. (2026). Mitigating chromium(VI) toxicity through microbial and biotechnological innovations: a critical review. *International Journal of Environmental Science and Technology*, *23*(5), 366. https://doi.org/10.1007/s13762-026-07141-0

Somanathan, T., Prasad, K., Ostrikov, K. K., Saravanan, A., & Krishna, V. M. (2015). Graphene oxide synthesis from agro waste. *Nanomaterials*, *5*(2), 826–834.

https://doi.org/10.3390/nano5020826

Tadjenant, Y., Dokhan, N., Barras, A., Addad, A., Jijie, R., Szunerits, S., & Boukherroub, R. (2020). Graphene oxide chemically reduced and functionalized with KOH-PEI for efficient Cr(VI) adsorption and reduction in acidic medium. *Chemosphere*, *258*, 127316. https://doi.org/10.1016/j.chemosphere.2020.127316

Tan, Y., Wang, J., Zhan, L., Yang, H., & Gong, Y. (2024). Removal of Cr(VI) from aqueous solution using ball mill modified biochar: multivariate modeling, optimization and experimental study. *Scientific Reports*, *14*(1), 4853. https://doi.org/10.1038/s41598-024-55520-9

Tattibayeva, Z., Tazhibayeva, S., Kujawski, W., Zayadan, B., & Musabekov, K. (2022). Peculiarities of adsorption of Cr(VI) ions on the surface of Chlorella vulgaris ZBS1 algae cells. *Heliyon*, *8*(9), e10468. https://doi.org/10.1016/j.heliyon.2022.e10468

Temesgen, M., Alemu, T., & Shasho, E. (2024). Heavy metals pollution and potential health risks: The case of the Koche river, Tatek industrial zone, Burayu, Ethiopia. *Journal of Toxicology*, *2024*(1). https://doi.org/10.1155/jt/9425206

Thangaraj, B., Mumtaz, F., Abbas, Y., Anjum, D. H., Solomon, P. R., & Hassan, J. (2023). Synthesis of graphene oxide from sugarcane dry leaves by two-stage pyrolysis. *Molecules*, *28*(8), 3329. https://doi.org/10.3390/molecules28083329

Tibebu, S., Kassahun, E., Ale, T. H., Worku, A., Sime, T., Berhanu, A. A., Akino, B., Hailu, A. M., Ayana, L. W., Shibeshi, A., Mohammed, M. A., Lema, N. K., Ammona, A. A., Tebeje, A., Korsa, G., Ayele, A., Nuru, S., Kebede, S., Ayalneh, S., Ashebir, H. (2024). The application of Rumex Abysinicus derived activated carbon/bentonite clay/graphene oxide/iron oxide nanocomposite for removal of chromium from aqueous solution. *Scientific Reports*, *14*(1), 19280. https://doi.org/10.1038/s41598-024-70238-4

Umejuru, E., Christopher, Prabakaran, E., & Pillay, K. (2023). Coal fly ash decorated with graphene and polyaniline nanocomposites for effective adsorption of hexavalent chromium and its reuse for photocatalysis. *ACS Omega*, *8*(20), 17523–17537. https://doi.org/10.1021/acsomega.2c05352

Weber, W. J., & Morris, J. C. (1963). Closure to "kinetics of adsorption on carbon from solution." *Journal of the Sanitary Engineering Division*, *89*(6), 53–55. https://doi.org/10.1061/JSEDAI.0000467

World Health Organization. (2008). *Guidelines for drinking-water quality: Third edition incorporating the first and second addenda* (Vol. 1). World Health Organization.

Wu, S., Wang, X., Ma, Y., & Ma, L. (2026). Red mud-based mil-53(fe) for the efficient adsorption of methylene blue: Preparation, adsorption performance, and mechanism. *ACS Omega*, *11*(10), 16128–16140. https://doi.org/10.1021/acsomega.5c11138

Xie, S. (2024). Water contamination due to hexavalent chromium and its health impacts: exploring green technology for Cr(VI) remediation. *Green Chemistry Letters and Reviews*, *17*(1). https://doi.org/10.1080/17518253.2024.2356614

Yuan, X., Li, J., Luo, L., Zhong, Z., & Xie, X. (2023). Advances in sorptive removal of hexavalent chromium (Cr(VI)) in aqueous solutions using polymeric materials. *Polymers*, *15*(2), 388. https://doi.org/10.3390/polym15020388

Zerin, N. H., Rasul, M. G., Jahirul, M. I., Sayem, A. S. M., Quadir, Z., & Haque, R. (2025). XRD Characterization of

activated carbons synthesized from tyre pyrolysis char via KOH activation. *Technologies*, *13*(12), 565. https://doi.org/10.3390/technologies13120565

Zulfiqar, U., Haider, F. U., Ahmad, M., Hussain, S., Maqsood, M. F., Ishfaq, M., Shahzad, B., Waqas, M. M., Ali, B., Tayyab, M. N., Ahmad, S. A., Khan, I., & Eldin, S. M. (2023). Chromium toxicity, speciation, and remediation strategies in soil-plant interface: A critical review. *Frontiers in Plant Science*, *13*. https://doi.org/10.3389/fpls.2022.1081624